Electron density distribution in paramagnetic and antiferromagnetic MnO: A γ-ray diffraction study

W. Jauch
Hahn-Meitner-Institut, Glienicker Strasse 100, D-14109 Berlin, Germany

M. Reehuis
Institut für Physik, EKM, Universität Augsburg, Universitätsstrasse 1, D-86159 Augsburg, Germany
(Received 6 September 2002; published 30 May 2003)

High-accuracy single-crystal structure factor data sets, up to $\sin\theta/\lambda = 1.6$ Å^{-1}, have been measured from MnO at 295 K and in the antiferromagnetic state at 15 K using 316.5-keV gamma radiation. In the rhombohedral low-temperature phase, monodomain formation was enforced by application of moderate stress. A detailed description of the electron-density distribution is derived in terms of a multipolar atomic deformation model. A substantial difference is observed between the *d*-orbital occupancies in the two magnetic phases. The Mn valence region shows considerable asphericity already in the cubic phase. In the antiferromagnetic state, distinct anisotropies are observed both in electron density and thermal vibrations, contrary to the common belief that the distortion from cubic symmetry is negligible. The $3d$ charge distribution is contracted by about 4% relative to the free atom. The total number of *d* electrons on Mn is found to be 4.74(2), in accordance with the magnetic moment derived from neutron diffraction. Special attention is devoted to Bader's atoms-in-molecules theory, which reveals the Mn-O interaction to be purely ionic. The implication for the interpretation of the superexchange mechanism is discussed.

DOI: 10.1103/PhysRevB.67.184420 PACS number(s): 71.20.-b, 61.50.Lt, 61.10.-i

I. INTRODUCTION

MnO is conceptually the simplest transition-metal monoxide, with Mn having a half filled $3d$ shell, and the spin subbands being either completely full or completely empty, so that a crystal field cannot split the orbital singlet. Though MnO is one of the most intensively studied compounds, both experimentally and theoretically, its electronic structure is still a subject of controversy.

Electron density is the fundamental independent variable of many-electron density-functional theory.[1] The spatial distribution of the electron density in the unit cell $\rho(\mathbf{r})$ is a physical observable that can be obtained from high-quality diffraction data. An accurate determination of the electron density represents a strong constraint for theoretical calculations and should thus be very valuable for a better characterization of this prototypic compound. The purpose of the present paper is to give a detailed exploration of the electronic charge density in paramagnetic and antiferromagnetic MnO obtained from extended sets of gamma-ray structure factors above and below the Néel temperature. We have found only one x-ray single-crystal study of MnO performed at room temperature but a quantitative assessment of the electron density is lacking.[2] Our investigation is a follow up to a previous γ-ray diffraction study of CoO.[3]

There are important differences between diffraction data recorded with x rays or synchrotron radiation and higher-energy gamma rays concerning potential sources of systematic errors.[4] With the use of a photon energy above 300 keV, the high-energy diffraction case is fully realized (photon energy » binding energy of *K*-shell electrons), and a structure factor accuracy at the 0.1% level is achievable, profiting from low absorption and extinction, no dispersion corrections, and reasonably large samples making surface effects negligible. The improvement in accuracy is also due to favorable experimental conditions besides energy, such as the perfect stability, monochromaticity, and homogeneity of the incident γ-ray beam. Single-crystal studies involving phase transitions with a lowering of symmetry need special precaution to keep the specimen untwinned. Domain formation is suppressed in the present study by the application of uniaxial pressure.

II. CRYSTAL STRUCTURE

At room temperature, MnO is paramagnetic and has NaCl structure (space group $Fm\bar{3}m$; $a = 4.4457$ Å).[5] The transition to the antiferromagnetic state at $T_N \simeq 120$ K is accompanied by a rhombohedral distortion with a contraction along the $\langle 111 \rangle$ direction. The resulting crystallographic symmetry is trigonal (space group $R\bar{3}m$) and the only threefold axis is the compression axis. At 10 K, the rhombohedral cell parameters are $a = 3.1336$ Å and $\alpha = 60.721°$.[5] For the present purpose, it is more convenient to use a hexagonal unit cell (three times the volume of the primitive rhombohedral cell) with the lattice constants $a = 3.1677$ Å and $c = 7.6336$ Å, and with Mn at $3a$ (0,0,0) and O at $3b$ (0,0,1/2).

In MnO, the magnetic structure is collinear and the spins are perpendicular to the triad axis. It has been pointed out that such a structure is inconsistent with a rhombohedral lattice.[6,7] The true symmetry should be lower than trigonal. In an effort to settle this issue we have performed powder-diffraction measurements (commercial sample of 99.99% purity), making use of the high-resolution powder diffractometer at BM1B (Swiss-Norwegian beamline), installed on a bending-magnet beamline at the European Synchrotron Radiation Facility. A partial powder pattern ($\lambda = 0.8$ Å) was measured at $T = 5$ K. Unfortunately, the angular resolution

was limited by the sample quality. The peak widths at low temperature increased by a factor of about 2 as compared to room temperature, which most likely arose from internal strain. Thus, no deviation from trigonal symmetry, resulting in additional peaks or unusual peak shapes, was perceptible.

A neutron powder-diffraction pattern at $T=4$ K was recorded on the two-axis diffractometer E9 of the BERII reactor (Hahn-Meitner-Institut, Berlin) using a wavelength of 1.7971 Å. The scattering angle range covered 10°–100°. From a full pattern Rietveld refinement, an ordered magnetic moment of $4.54(5)\mu_B$ per manganese was found, which is in good agreement with the previously reported value of $4.58(3)\mu_B$.[6]

III. EXPERIMENTAL AND DATA REDUCTION

The single crystal used in the present investigation was a cuboid of dimensions $2.89\times2.95\times3.08$ mm^3 containing a (111) surface, purchased from MaTecK/Jülich (Germany). Bragg intensities have been measured on the gamma-ray diffractometer at the Hahn-Meitner-Institut. This diffractometer works with a commercially available ^{192}Ir source of 200 Ci activity and a half-life of 74.2 days. The most intense line of the ^{192}Ir spectrum at 316.5 keV (0.0392 Å) was used. The diffracted gamma rays were registered in ω-step scan mode with an intrinsic Ge planar detector. Data sets were collected at room temperature (RT) and at 15 K [low temperature (LT)].

Below T_N, crystallographic domains can occur, resulting from twinning of the crystal according to the four equivalent [111] contraction axes. Domain formation can be prevented by stress along a cubic ⟨111⟩ direction. At LT, the sample was forced into a monodomain by an applied stress of approximately 200 bar. The force was controlled by means of a steel spring, thereby eliminating uncontrollable thermal stress during the cooling down process.

Data sets were collected up to $\sin\theta/\lambda=1.6$ Å^{-1}. The completeness in independent reflections was 100% at RT and 86% at LT, where the weakest reflections were not measured. An absorption correction was carried out ($\mu=0.534$ cm^{-1}), resulting in a transmission range from 0.852 to 0.866. At RT, 436 diffraction data of high precision were averaged over symmetry-related observations to 106 independent reflections with $\Sigma\sigma(I)/\Sigma I=0.0070$. At LT, 420 observations of somewhat inferior precision were averaged to 267 independent data with $\Sigma\sigma(I)/\Sigma I=0.023$. The sets of independent data were used for the further study. The data reductions were carried out using the XTAL suite of crystallographic programs.[8] Profile fits of the rocking curves at both temperatures revealed a Gaussian shape with a full width at half maximum (FWHM) of 7′, which is considerably broader than the triangular primary beam divergence with a FWHM of 3.5′. The crystal mosaic distribution is thus of a Gaussian type with a FWHM of 6.1′.

The RT data had to be corrected for the contribution of inelastic thermal diffuse scattering (TDS) to the total intensity. The formalism of Skelton and Katz[9] was applied, using elastic constants from Hearmon[10] and the instrumental parameters defining the sampled volume in reciprocal space: ω-scan peak width=0.5°, full circular detector window =0.46°. The TDS contribution reached 12% at $\sin\theta/\lambda=1.6$ Å^{-1}.

IV. RESULTS

Structure refinements were performed with the program system VALRAY,[11] minimizing $\chi^2=\Sigma w(|F_o|^2-|F_c|^2)^2$, where F_o and F_c are the observed and calculated structure factors, respectively. The observations were weighted solely by their counting-statistical variances.

A. Independent-atom model (IAM)

Scattering factors for neutral Mn and O atoms (the free O^{2-} ion is unstable) were calculated from the Hartree-Fock (HF) wave functions given in Clementi and Roetti.[12] The fit parameters were the scale factor of the observed intensities, a secondary extinction parameter [Gaussian mosaic width parameter $g=0.6643$/FWHM (rad)], and the mean-square amplitudes of vibration of the two atoms. In the antiferromagnetic phase the site symmetry is reduced, and each atom has two independent vibrational components. In order to reduce the influence of charge-density deformations in the outer shells, high-order refinements were carried out, taking into account only reflections with $\sin\theta/\lambda>0.7$ Å^{-1}. The final scale factor was fixed in later refinements with improved scattering models. To test for deviations from ideal stoichiometry, in particular, for metal deficiency, the occupancy of the manganese site was allowed to vary in a high-order refinement, resulting in an ideal value of 1.000(2).

The secondary extinction factor for the strongest reflection of the RT data set, calculated with the Becker-Coppens formalism[13] ($g=370$ rad^{-1}), is $y(200)=0.970$ ($y=I_{\rm obs}/I_{\rm kin}$, where $I_{\rm obs}$ and $I_{\rm kin}$ are the observed intensity and its kinematic value, respectively). The minimum extinction length amounts to 80 μm, much larger than the expected size of perfect domains, so that primary extinction effects are absent. The large mosaicity in connection with the high gamma energy used in this study thus assures almost pure kinematic scattering conditions.

B. Multipole model

In the aspherical atom multipole model the electron-density distribution is projected onto a small finite basis set of real spherical harmonic functions centered at the nuclear positions with the local density rigidly following the motion of its associated nucleus.[14] The model is thus based on the assumption that the electron-density distribution in the unit cell may be decomposed into contributions allocated to its constituent atoms. For manganese, the atomic density is represented as

$$\rho_{\rm Mn}(\mathbf{r})=\rho_{\rm Mn,core}(r)+\kappa^3R_{3d}(\kappa r)\sum_{l=0}^{4}\sum_{m=0}^{l}P_{lm\pm}y_{lm\pm}(\mathbf{r}/r).$$

With the site symmetry $m\bar{3}m$ of the rocksalt structure the only allowed higher multipole is the fourth-order cubic har-

TABLE I. Quality of fit for the various scattering models. Np = Number of adjustable parameters. The numbers of unique reflections are 106 at RT and 267 at 15 K. In all cases, the scale factor was fixed to the value obtained from high-order IAM refinements.

		IAM	Monopoles	Multipoles
$T=295$ K	χ^2	652.6	184.3	148.2
	Np	3	6	8
$T=15$ K	χ^2	1228.0	886.6	516.1
	Np	5	8	14

monic, which is a linear combination of y_{40} and y_{44+}. In the rhombohedral phase the site symmetry is $3m$ and the contributing multipoles are $(l,m)=(0,0)$, (2,0), (4,0), and (4,3+).

For oxygen,

$$\rho_{\mathrm{O}}(\mathbf{r})=\rho_{\mathrm{O,core}}(r)+P_{\mathrm{O,val}}\kappa^3\rho_{\mathrm{O,val}}(\kappa r)+\sum_{l=2}^{4}\kappa^3 R_l(\kappa r)\sum_{m=0}^{l}P_{lm\pm}y_{lm\pm}(\mathbf{r}/r).$$

$\rho_{\mathrm{Mn,core}}$, $\rho_{\mathrm{O,core}}$, and $\rho_{\mathrm{O,val}}$ are unperturbed HF electron densities of the appropriate atomic orbitals. $\rho_{\mathrm{O,val}}$ is the average of the $2s$ and $2p$ orbitals, normalized to one electron. For Mn, the square of the radial part of the $3d$ canonical HF orbitals is used to construct both monopole and multipoles, reflecting the fact that the deformation is essentially due to different d-orbital occupancies. The radial function for the $l=2$ pole of oxygen consists of a $2p2p$ atomic-orbital product. The $l=4$ radial function of oxygen is a single Slater function $r^4\exp(-\alpha r)$, with the standard exponent $\alpha=4.50$ bohr^{-1}. The κ parameters allow for expansion ($\kappa<1$) or contraction ($\kappa>1$) of the radial functions. $P_{\mathrm{O,val}}$ and $P_{lm\pm}$ are variable population coefficients. Monopolar populations were constrained to ensure electroneutrality of the crystal. The spherical harmonics are expressed relative to a global Cartesian frame, which is oriented parallel to the unit-cell axes for the cubic phase. In the hexagonal cell, the z axis is along the principal symmetry axis [001], the x axis is along [210], and y is chosen along [010] so that one of the ligands lies in the xz plane. The y_{43+} multipole function is defined with positive lobes pointing towards the ligand atoms.

In Table I, the quality of fit is given for the various scattering models. It is evident that the data contain information going beyond the IAM. A large improvement of fit is already obtained on the introduction of charge transfer and valence-shell expansion/contraction. The very high precision of the RT data is reflected by the large value of χ^2 for the IAM. The results of the multipole refinements are listed in Table II. Note that the normalization condition for the aspherical density functions is such that the coefficients $P_{lm\pm}$ correspond to the local electrostatic moments in angstrom units

Adjustment of the secondary extinction parameter gives $g=300(22)$ rad^{-1} at RT, in fair accordance with the observed value. The refined value at LT amounts to $g=184(63)$ rad^{-1}. Extinction factors calculated with the Becker-Coppens formalism are listed in Table III for the lowest-order RT structure factors that have been measured to a statistical precision below 0.1%.

TABLE II. Results from multipole refinements of paramagnetic and antiferromagnetic MnO. $U_{\parallel}$ and $U_{\perp}$ denote mean-square vibrational amplitudes parallel and perpendicular to the threefold axis.

		295 K	15 K
Mn	$U_{\parallel}$ (Å^2)	0.005 63(1)	0.002 38(3)
	$U_{\perp}$ (Å^2)	0.005 63(1)	0.002 10(2)
	κ	1.050(5)	1.037(3)
	P_{00} ($\lvert e\rvert$)	4.74(2)	4.75(2)
	P_{20} ($\lvert e\rvert$Å^2)		0.70(5)
	P_{40} ($\lvert e\rvert$Å^4)	0.18(5)	0.20(5)
	P_{43+} ($\lvert e\rvert$Å^4)		−1.46(17)
O	$U_{\parallel}$ (Å^2)	0.005 84(6)	0.003 78(18)
	$U_{\perp}$ (Å^2)	0.005 84(6)	0.003 40(10)
	κ	0.980(4)	0.978(3)
	P_{val} ($\lvert e\rvert$)	6.26(2)	6.25(2)
	P_{20} ($\lvert e\rvert$Å^2)		0.05(6)
	P_{40} ($\lvert e\rvert$Å^4)	0.04(7)	0.46(8)
	P_{43+} ($\lvert e\rvert$Å^4)		−0.92(29)

The static model densities, with the Debye-Waller factor omitted, were evaluated in direct space and checked for unphysical negative densities; they proved to be positive everywhere in the unit cell. Figures 1 and 2 show the static deformation densities (aspherical components only) calculated in direct space. The regions of excess density near the Mn atom reflect the preferential occupancy of certain d orbitals, whereas the destabilized orbitals are manifested by regions of electron deficiency. A detailed discussion of the deformation maps is given below.

It has been checked whether the current model density is flexible enough to represent all systematic features available in the RT data. It turned out that inclusion of $l=6$ terms for Mn or anharmonic terms in the Debye-Waller factors yielded only insignificant improvements of fit. Since the $4s$-orbital contributes very little to the scattering its population cannot be reliably determined, and the number was kept equal to 2.

C. Analysis of the bonding state

The quantum theory of atoms in molecules (AIM), developed by Bader,[15] uses the electron density as its starting point, and provides a natural characterization of the nature of the interactions present in an assembly of atoms. Presence and classification of a chemical bond are based on the existence of a saddle point (bond critical point $\mathbf{r}_c$) of the electron density between two linked atoms and on the value of the associated Laplacian $\nabla^2\rho(\mathbf{r}_c)=\lambda_1+\lambda_2+\lambda_3$ (λ_i are the eigenvalues of the Hessian of the density; λ_3 designates the component along the internuclear axis). A large negative value of $\nabla^2\rho(\mathbf{r}_c)$ is typical for shared-electron interaction (covalent bond), whereas unshared-electron interaction (ionic bond) is characterized by $\nabla^2\rho(\mathbf{r}_c)\gg 0$ combined with a small value of $\rho(\mathbf{r}_c)$.

Additional, more quantitative information about the bond type can be obtained by consideration of energetic aspects.

TABLE III. Low order structure factors of MnO in units of electrons per cell ($T=295$ K) with the extinction coefficients y referring to the reduction in F^2.

hkl	F_o	F_c	y
111	52.29(3)	52.29	0.990
200	90.67(5)	90.66	0.974
220	73.05(8)	72.97	0.988
311	39.76(6)	39.69	0.998
222	61.12(4)	61.19	0.994
400	53.05(5)	53.13	0.996

$R(F)=\Sigma|F_o-F_c|/\Sigma|F_o|=0.000\,81$
$R(\sigma)=\Sigma\sigma(F_o)/\Sigma|F_o|=0.000\,81$

The Laplacian function of the electron density is connected with the electronic kinetic-energy density $G(\mathbf{r})$ and the electronic potential-energy density $V(\mathbf{r})$ by the local virial theorem[15] $2G(\mathbf{r})+V(\mathbf{r})=(\hbar^2/4m)\nabla^2\rho(\mathbf{r})$. At $\mathbf{r}_c$, the kinetic energy per electron, the ratio $G(\mathbf{r}_c)/\rho(\mathbf{r}_c)$, should be less than unity for covalent interactions and greater than unity for ionic interactions (when expressed in atomic units). Abramov[16] recently proposed an expression for $G(\mathbf{r}_c)$ in terms of $\rho(\mathbf{r}_c)$ and $\nabla^2\rho(\mathbf{r}_c)$, thus allowing its evaluation from the model electron density. The potential-energy contribution and consequently the total electronic energy density $H(\mathbf{r}_c)=G(\mathbf{r}_c)+V(\mathbf{r}_c)$ follow from the local virial theorem.

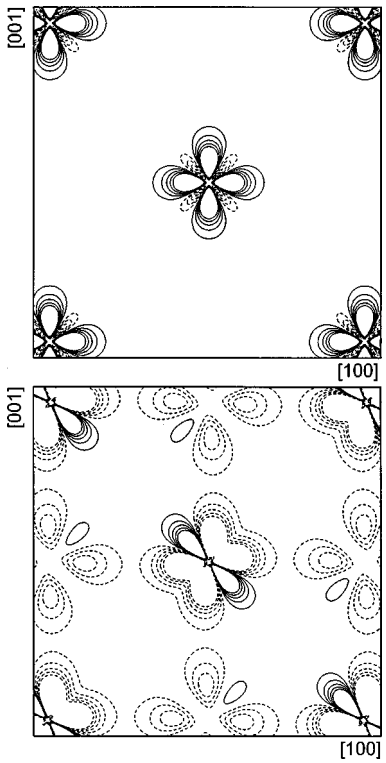

FIG. 1. Aspherical contributions to the static model density in the cubic (100) plane. Top: paramagnetic MnO with a density range from -0.22 to 0.89 eÅ^{-3}. Bottom: antiferromagnetic MnO with a density range from -1.82 to 1.29 eÅ^{-3}. Mn is located in the center and the corners of the maps. Solid lines represent positive regions; and dashed lines negative regions in steps of 0.05 eÅ^{-3}. The zero contour is omitted. The densities are truncated at ±0.25 eÅ^{-3}.

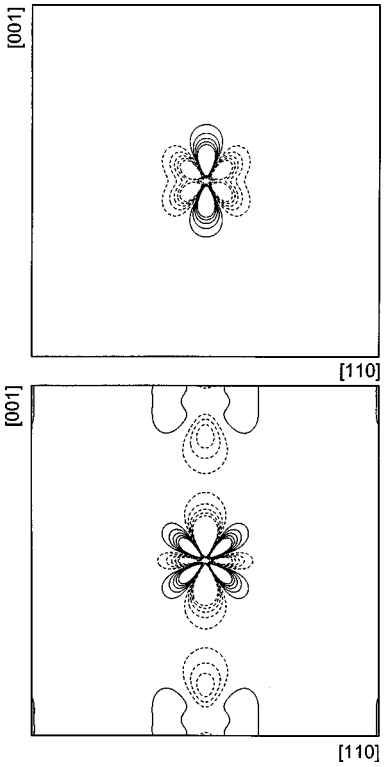

FIG. 2. Aspherical contributions to the static model density in the cubic (110) plane. Top: paramagnetic MnO with a density range from -0.59 to 0.88 eÅ^{-3}. Bottom: antiferromagnetic MnO with a density range from -1.73 to 0.71 eÅ^{-3}. Mn is located in the center of the map. Contours are as in Fig. 1.

The characteristics of the bond critical points are listed in Table IV. $G(\mathbf{r}_c)$ was obtained from a series expansion around the Thomas-Fermi result, which is a suitable approximation in the internuclear region where $\rho(\mathbf{r})$ varies slowly: $G(\mathbf{r}_c)=2.8713[\rho(\mathbf{r}_c)]^{5/3}+0.166\,67\nabla^2\rho(\mathbf{r}_c)$ with all quantities expressed in atomic units.[16] From inspection of Table IV, the bonding state in MnO is evidenced as being purely ionic. The corresponding values resemble those of sodium chloride,[16] often regarded as the prototypical ionic compound. It is found that $H(\mathbf{r}_c)\cong0$, a result which has also been obtained with CoO. It has been demonstrated by Cremer and Kraka[17] that for a covalent bond, $H(\mathbf{r}_c)$ is dominated by $V(\mathbf{r}_c)$ and is thus largely negative. Concerning the ionic bonding interaction the situation is less clear with assertions in the literature suggesting that in this case $G(\mathbf{r}_c)$ will dominate over $V(\mathbf{r}_c)$, thus leading to positive values of $H(\mathbf{r}_c)$.[18] However, our experimental results strongly suggest the ionic bond to be characterized by the exact balance of the two local energy densities.

V. DISCUSSION

A. Vibrational parameters

The mean-square amplitudes of vibration at RT are almost the same for both atoms, $U(\mathrm{Mn})/U(\mathrm{O})=0.964(10)$. It has

TABLE IV. Characteristics of the bond critical points in paramagnetic and antiferromagnetic MnO. Values of ρ are in e Å^{-3}; values of $\nabla^2\rho$ and λ_i are in e Å^{-5}. G, G/ρ, and V are given in atomic units.

$\mathbf{r}_c$	$\rho(\mathbf{r}_c)$	$\nabla^2\rho(\mathbf{r}_c)$	$\lambda_{1,2,3}$	$G(\mathbf{r}_c)$	$G(\mathbf{r}_c)/\rho(\mathbf{r}_c)$	$V(\mathbf{r}_c)$
$Fm\bar{3}m$						
0.2490(3), 0, 0	0.335(1)	5.09(3)	−1.25(1) −1.25(1) 7.58(2)	0.0544(2)	1.097(5)	−0.0560(6)
$R\bar{3}m$						
0.348(6), 0.174(3), 0.423(4)	0.285(4)	4.95(12)	−0.65(6) −0.58(5) 6.19(9)	0.0490(9)	1.161(23)	−0.0465(22)

been predicted that once the temperature becomes comparable to the Debye temperature Θ_D, both atoms of a binary compound with a cubic crystal structure should vibrate equally, irrespective of their masses.[19] From the two sound velocities one finds $\Theta_D = 350$ K, which is sufficiently close to the temperature of the experiment. This qualitative understanding of the vibrational behavior fails, however, in the case of cubic CoO, where $U(\mathrm{Co})/U(\mathrm{O}) = 0.80(2)$ at 305 K and $\Theta_D = 340$ K. The proximity of the magnetic phase transition in CoO ($T_N \simeq 290$ K) might account for the failure of the prediction from lattice-dynamical considerations.

The vibrational parameters obtained in this work are considerably smaller than the values reported by Sasaki, Fujino, and Takeuchi[2] from an x-ray study at 297 K, $U(\mathrm{Mn}) = 0.007\,81(6)$ and $U(\mathrm{O}) = 0.009\,12(25)$ Å^2. The difference between U(gamma ray) and U(x ray) is of the same order as the difference for CoO reported in Ref. 3. The discrepancy is due to the reduced monochromaticity of a graphite monochromated x-ray beam.[20] It contains a bremsstrahlung component with a large wavelength spread that fully contributes to the measured intensity at low Bragg angles and is progressively truncated at higher angles. The contribution of the bremsstrahlung depends on the tube voltage and leads to vibrational parameters that are systematically too large. The spectral width of the 316.5-keV photon beam is $\Delta\lambda/\lambda = 10^{-6}$ and no monochromator is needed.

At LT, the two atoms vibrate distinctly differently, roughly according to the corresponding mass ratio. Despite the relatively small deviation from cubic symmetry the anisotropy of the zero-point mean-square amplitudes is highly significant for Mn. The vibrations along the threefold axis are larger than in the orthogonal plane: $U_\parallel/U_\perp = 1.13(2)$. For O, the same result is obtained, though with increased uncertainty: $U_\parallel/U_\perp = 1.11(6)$. In antiferromagnetic CoO, the corresponding anisotropy ratio amounts to 1.16(5) for Co. The experimental finding supports a recent theoretical investigation of MnO in which it was argued that the antiferromagnetic ordering by itself induces a noncubic behavior of some nonmagnetic properties.[21]

Isotropic mean-square amplitudes of vibration have been calculated by Hewat using a simple rigid-ion model (reported in Ref. 22). The corresponding values are $U(\mathrm{Mn}) = U(\mathrm{O}) = 0.0061$ Å^2 at RT and $U(\mathrm{Mn}) = 0.0019$ Å^2, $U(\mathrm{O}) = 0.0034$ Å^2 at LT, respectively. The calculated values are rather close to our experimental results.

B. Monopole parameters

Within standard deviations, the monopole parameters are the same at the two temperatures. Pronounced deviations from the independent-atom values are observed. The manganese valence shell is contracted by about 4%, whereas the oxygen L shell exhibits an expansion of 2%. The expansion/contraction resembles that found for CoO.

The valence electron population of oxygen is 6.25, corresponding to a net donation of 0.25 electrons from the manganese atom. The charge transfer should be invariant with respect to the magnetic phase. It is worth noting that this important constraint is quantitatively satisfied. The radial scaling parameters are consistent with the charge transfer. A more positive atom, such as Mn, is expected to contract in view of the decreased screening of the nuclear charge. The net charges refer to the total charge content in the monopole functions which extend from zero to infinity in the radial coordinate.

The total number of d electrons on Mn is found to be significantly smaller than the formal value of 5. In MnO, the orbital magnetic moment is expected to be absent, which was recently confirmed using magnetic x-ray diffraction.[23] The population of the monopolar deformation function can therefore be compared straightforwardly with the magnetic moment on (high-spin) manganese. To deduce the absolute moment, the zero-point spin deviation has to be taken into consideration. It was calculated by Lines and Jones[24] to be 3.0% for MnO. The absolute magnetic moment as obtained from neutron diffraction is thus $4.7\mu_B$. The close agreement between the γ-ray and neutron results supports the reliability of the multipole partitioning leading to physically meaningful atomic charges. Finally, it is noteworthy that the spin magnetic moment can be deduced from a charge scattering experiment.

Complementary information about the spatial extent of the unpaired electrons is also accessible from magnetic neutron diffraction. A radial contraction of the $3d$ charge distribution was found in CoO and NiO from single-crystal unpolarized neutron studies, and it was concluded that, in general, the crystalline environments tend to contract the magnetization density distributions of the magnetic electrons.[25] Accurate powder-diffraction measurements of the spherical mag-

netic form factor of Mn in MnO, however, reveal close agreement with the independent-atom case.[22] This result is not consistent with our findings. We can offer no explanation for the discrepancy except to point out that the γ-ray data are more directly related to the radial parameter whereas the neutron data require a variety of treatments, such as separation of overlapping magnetic and nuclear intensities and gauge of the magnetic intensities. It should be noted here that retrieving the magnetic form factor is a far more ambitious type of experiment than determination of the magnetic moment.

It is interesting to compare the experimental local magnetic moment with *ab initio* calculations. Several improved density-functional schemes have been applied to MnO, including the local spin-density (LSD) approximation also taking into account the Hubbard U term (LSD+U) and the generalized gradient approximation (GGA). The following values have been reported for the magnetic moment (μ_B) on Mn: 4.61 (LSD+U),[26] 4.85 (LSD+U),[27] 4.68 (LSD+U),[28] 4.15 (GGA),[29] and 4.47 (GGA).[30] In a recent study[31] using the periodic HF scheme a value of 4.92 was obtained. Although the theoretical data scatter quite a bit, agreement between the calculated noninteger Bohr magneton numbers based on the LSD+U and the experimental ones is fairly good.

The AIM theory[15] provides a unique partitioning of the total charge density into a disjoint set of mononuclear regions, termed atomic basins (Ω), which are bound by a surface whose flux of the gradient vector field $\nabla\rho(\mathbf{r})$ vanishes. The electron population of an atom is obtained by integration of $\rho(\mathbf{r})$ over its basin. The net atomic charge $q(\Omega)$ is the difference between the nuclear charge and the integrated electron population. Application of the space partitioning algorithm by Flensburg and Madsen[32] gives $q(\mathrm{Mn})=-q(\mathrm{O})=1.23|e|$, and $V(\mathrm{Mn})=10.40$ Å^3 and $V(\mathrm{O})=11.57$ Å^3. The summations of the atomic volumes and populations over the unit cell reproduce V_c and $F(000)$ to within 0.01%. As in the case of CoO, the net atomic charges are considerably smaller than the formal value of 2. Though the AIM charges have a clear and rigorous significance, they are not amenable to comparison with the results of other physical methods. This situation is quite different from the partitioning scheme based on the $3d$-shell charges, as has been demonstrated above.

C. *d*-orbital populations of Mn

The $3d$-electron density may be described by multipole functions (as above) or, alternatively, it may be expressed in terms of the atomic orbitals d_i. There is a linear relationship between the multipole population and the *d*-orbital population coefficients (provided the expansion is truncated at $l=4$ and overlap between metal and ligand orbitals is negligible).[33] In the cubic field, the *d* orbitals split into e_g (x^2-y^2, z^2) orbitals pointing towards the ligands and t_{2g} (xy, xz, yz) orbitals pointing between them.

On the lowering of the symmetry from cubic to trigonal, the coordination octahedron of the metal atom has symmetry $\bar{3}m$. Two of its faces are perpendicular to the 3 axis; the other six faces are equivalent and oblique to the threefold axis. Therefore, the t_{2g} orbitals of cubic symmetry split into a single a_g with its lobes pointing along the threefold axis and a doubly degenerate e_g level, whereas the original e_g orbitals retain their symmetry characteristic and are now termed e_g'.[34] The symmetry-adapted set that correlates with the octahedral orbitals is given by $a_g=d_{z^2}$, $e_{g+}=ad_{x^2-y^2}-bd_{xz}$, $e_{g-}=ad_{xy}+bd_{yz}$, $e_{g+}'=bd_{x^2-y^2}+ad_{xz}$, and $e_{g-}'=bd_{xy}-ad_{yz}$, where $a=\sqrt{2/3}$ and $b=\sqrt{1/3}$. Here, the threefold axis is taken as the z direction, and the x axis is chosen so that one of the ligands lies in the xz plane. The signs of the linear combination imply a positive e_g' lobe in the positive xz quadrant. The angular distribution of the $3d$ electrons is then given as

$$\rho_{3d}=P_1(a_g)^2+\frac{1}{2}P_2[(e_{g+})^2+(e_{g-})^2]+\frac{1}{2}P_3[(e_{g+}')^2+(e_{g-}')^2]+\frac{1}{2}P_4(e_{g+}e_{g+}'+e_{g-}e_{g-}').$$

P_1, P_2, and P_3 are the number of electrons in the corresponding orbitals. The additional cross product term is present because the e_g and e_g' orbitals belong to the same symmetry representation and may mix; the parameter P_4 is related to the extent of mixing. It should be noted that the orbital-multipole matrix $\mathbf{M}^{-1}$ for trigonal symmetry that is given in Ref. 35 is incorrect (two elements of the inverse matrix $\mathbf{M}$ are too large by a factor of 2). The correct matrix is therefore given in Table V. The populations of the $3d$ orbitals derived from the Mn multipole parameters are listed in Table VI.

TABLE V. Orbital-multipole matrix for trigonal symmetry that should replace Table 8.7.3.5.(b) in Ref. 35. The matrix differs from that used for the calculation of Table VI because of differences in the normalization of the density functions.

	P_{00}	P_{20}	P_{40}	P_{43+}
$P_1(a_g)$	0.200	1.039	1.396	0.00
$P_2(e_g)$	0.400	−1.455	0.00	−3.554
$P_3(e_g')$	0.400	0.416	−1.396	3.554
$P_4(e_ge_g')$	0.00	−2.646	1.974	2.513

TABLE VI. $3d$-orbital populations on Mn; in the hexagonal cell z is along [001] and x is chosen so that one of the ligands lies in the xz plane.

Orbital	$m\bar{3}m$	Orbital	$\bar{3}m$
e_g	2.11(4)	e_g'	1.25(8)
t_{2g}	2.63(5)	e_g	2.23(8)
		a_g	1.27(4)
		e_ge_g'	−0.78(8)
Total d	4.74(2)		4.75(3)

The *d*-orbital analysis clearly reveals the crystal-field splitting. Surprisingly, in the cubic crystal field the ratio of the e_g/t_{2g} population is 0.80, which is considerably larger than the ideal 2:3 ratio corresponding to a spherical high-spin Mn atom. For this reason, the e_g orbitals show up as peaks in Figs. 1 and 2 (top) whereas the t_{2g} orbitals correspond to the regions of charge deficiency relative to the spherical atom. Our experimental result is in qualitative agreement with recent theoretical work (LDA+U method[36]) where it follows that the charge rearrangement between e_g and t_{2g} leads to a reduction of the large value of the on-site $3d$ Coulomb repulsion. A similar situation has already been noted in cubic CoO, where the experimental value of $e_g/t_{2g}=0.51$ is also larger than the nominal 2:5 ratio.

The populations at LT are very different from those predicted from electrostatic considerations. The Mn-O distance of 2.223 Å in the cubic phase is elongated to 2.228Å in the rhombohedral phase. According to crystal-field theory, the e_g' orbitals pointing along the ligands should therefore show little difference in population compared to the cubic phase. Actually, it is found that 0.9 electrons are removed from e_g' into e_g. The e_g' orbital is now depopulated relative to the spherical atom. The larger occupancy of the e_g orbital than the e_g' orbital is related to the negative P_{43+} population. For exact cubic symmetry the relative occupancies of the isolated atom are 40% (e_g'), 40% (e_g), and 20% (a_g). The experimental result reveals strong anisotropy with 26% (e_g'), 47% (e_g), and 27% (a_g). The e_g e_g' cross term is highly significant, which reflects the considerable amount of orbital mixing. In Figs. 1 and 2 (bottom), the regions of electron depletion around the manganese atom display the e_g' orbitals, whereas the maxima correspond to e_g. The electron withdrawal along the Mn-O bond is qualitatively similar to the distribution in antiferromagnetic CoO. The aspherical component of oxygen, however, is almost an order-of-magnitude smaller in MnO than it is in CoO. The observed anisotropy in electron subshell population is at variance with the common view according to which lower than cubic effects can be ignored in antiferromagnetic MnO.

In the case of magnetically ordered CoO, the observed $3d$ occupancies allowed an unambiguous assignment of spin magnetic moment to the individual orbitals. In MnO, however, the orbital populations are fractional, which prevents a corresponding assortment. Noninteger orbital occupancies will result when the electronic ground state is inaccurately described by a single configuration, and a better description is in terms of configuration interaction, a mixture of several configurations.

D. Aspects of superexchange

A decrease of the magnetic ion moment compared to the free ion moment due to a partial transfer to the ligands is not unexpected in antiferromagnetic salts. It is commonly interpreted in terms of a molecular-orbital model.[37] The admixture of ligand orbitals into the central ion *d* orbitals may lead to an overlap density as well as to a spin transfer from the metal to the ligand. The admixture parameters are small and the covalency effect is treated as a small perturbation of the ionic configuration. The admixture or covalency parameters in MnO are of the order of only 1%.[22]

A covalent coupling between ligands and the *d* electrons of the magnetic ions is essential for the superexchange mechanism.[38,39] In this scheme, a configuration interaction is set up involving excited states. Examination of a cluster model consisting of three sites, with the ground state Mn^{2+}-O^{2-}-Mn^{2+}, and virtual transitions to the three excited configurations Mn^{+}-O^{-}-Mn^{2+}, Mn^{2+}-O^{-}-Mn^{+}, and Mn^{+}-O-Mn^{+}, leads to an energy shift of the ground state, part of which depends on the relative spin orientations of the manganese and can be expressed in the Heisenberg form; that is, a substitute Hamiltonian of the exchange type is developed. Overlap between cation and anion orbitals is fundamental to the theory. The present study, however, ascertains the absence of any shared-electron interaction between the Mn and O atoms.

An alternative approach which involves electron correlation rather than exchange to treat the antiferromagnetic spin coupling has been proposed by Slater.[40] He pointed out that in the transition-metal monoxides an oxygen ion is acted on by three neighboring metal ions in one plane with spin up and three others in the opposite plane with spin down so that there will be no net spin polarization of the anion (as the model of a linear chain of ions suggests on account of the exclusion principle). An individual oxygen orbital with spin up, however, will be exposed to a lower potential in the plane of Mn spin-down ions and a higher potential in the plane of Mn spin-up ions. There will be the opposite effect on oxygen spin-down orbitals. As a result, the charge distribution of oxygen will be distorted, such that one side of it will have an excess of spin-up charge, the other an excess of spin-down charge. The antiferromagnetic configuration is thus stabilized by the deformation of the outer electron shell of oxygen. Both an expansion and a deformation of the oxygen valence shell are clearly revealed in the magnetically ordered state. The view that electron correlation rather than exchange effects are responsible for the magnetic ordering in MnO is therefore not inconsistent with the present study. As already mentioned earlier, however, the oxygen deformation is almost an order-of-magnitude smaller than the corresponding one in CoO.

VI. CONCLUSION

A detailed investigation of the electron-density distribution in paramagnetic and antiferromagnetic MnO has been presented. The very short γ-ray wavelength of 0.0392Å, in connection with a sample of suitable mosaicity around 10′, allowed almost extinction-free measurements. Employment of the multipole expansion formalism to account for crystal bonding deformations brought large improvements compared to the independent-atom model, and yielded a reduced chi square close to 1, practically exhausting the accuracy of the data. The main features discovered are the following. (i) The $3d$ valence shell is contracted by about 4%. (ii) Substantial differences occur between the electron-density distribution in the two magnetic phases. (iii) In the cubic phase, a nonspherical distortion of the half filled *d* shell is revealed. (iv)

In the antiferromagnetic phase, both the electron density and the thermal vibrations exhibit distinct anisotropy, substantiating a noncubic behavior. (v) The magnetic moment inferred from charge scattering agrees well with neutron diffraction. (vi) The Mn-O interaction is evidenced to be purely ionic, which conflicts with the common interpretation of the superexchange phenomenon.

ACKNOWLEDGMENT

We are grateful to Dr. P. Pattison for collecting the synchrotron powder-diffraction data, Dr. H.-J. Bleif for helpful discussions and support, H. O. Sørensen for evaluation of the AIM charges, and Dr. D. Többens for assistance during the neutron powder experiment.

[1] P. Hohenberg and W. Kohn, Phys. Rev. B **136**, B864 (1964).
[2] S. Sasaki, K. Fujino, and Y. Takeuchi, Proc. Jpn. Acad., Ser. B: Phys. Biol. Sci. **55**, 43 (1979).
[3] W. Jauch and M. Reehuis, Phys. Rev. B **65**, 125111 (2002).
[4] W. Jauch, J. Phys. Chem. Solids **62**, 2103 (2001).
[5] B. Morosin, Phys. Rev. B **1**, 236 (1970).
[6] A. K. Cheetham and D. A. Hope, Phys. Rev. B **27**, 6964 (1983).
[7] H. Shaked, J. Faber, and R. L. Hitterman, Phys. Rev. B **38**, 11 901 (1988).
[8] Computer code XTAL 3.4, user's manual, edited by S. R. Hall, G. S. D. King, and J. M. Stewart (University of Western Australia, Perth, Australia, 1995).
[9] E. F. Skelton and J. L. Katz, Acta Crystallogr., Sect. A: Cryst. Phys., Diffr., Theor. Gen. Crystallogr. **A25**, 319 (1969).
[10] R. F. S. Hearmon, in *Numerical Data and Functional Relationships in Science and Technology*, edited by K.-H. Hellwege, Landolt-Börnstein New Series, Group III, Volume 11 (Springer-Verlag, Berlin, 1979).
[11] R. F. Stewart, M. Spackman, and C. Flensburg, computer code VALRAY, user's manual (Carnegie-Mellon University, Pittsburgh, Pennsylvania, and University of Copenhagen, Copenhagen, Denmark, 2000).
[12] E. Clementi and C. Roetti, At. Data Nucl. Data Tables **14**, 177 (1974).
[13] P. Becker and P. Coppens, Acta Crystallogr., Sect. A: Cryst. Phys., Diffr., Theor. Gen. Crystallogr. **A31**, 417 (1975).
[14] R. F. Stewart, Acta Crystallogr., Sect. A: Cryst. Phys., Diffr., Theor. Gen. Crystallogr. **A32**, 565 (1976).
[15] R. F. W. Bader, *Atoms in Molecules: A Quantum Theory* (Clarendon, Oxford, 1990).
[16] Yu. A. Abramov, Acta Crystallogr., Sect. A: Found. Crystallogr. **A53**, 264 (1997).
[17] D. Cremer and E. Kraka, Angew. Chem., Int. Ed. Engl. **23**, 67 (1984).
[18] P. Macchi, D. M. Proserpio, and A. Sironi, J. Am. Chem. Soc. **120**, 13 429 (1998).
[19] C. Huiszoon and P. P. M. Groenewegen, Acta Crystallogr., Sect. A: Cryst. Phys., Diffr., Theor. Gen. Crystallogr. **A28**, 170 (1972).
[20] B. Rousseau, S. T. Maes, and A. T. H. Lenstra, Acta Crystallogr., Sect. A: Found. Crystallogr. **A56**, 300 (2000).
[21] S. Massidda, M. Posternak, B. Baldereschi, and R. Resta, Phys. Rev. Lett. **82**, 430 (1999).
[22] A. J. Jacobson, B. C. Tofield, and B. E. F. Fender, J. Phys. C **6**, 1615 (1973).
[23] W. Neubeck, C. Vettier, F. de Bergevin, F. Yakhou, D. Mannix, L. Ranno, and T. Chatterji, J. Phys. Chem. Solids **62**, 2173 (2001).
[24] M. E. Lines and E. D. Jones, Phys. Rev. A **139**, A1313 (1965).
[25] D. C. Khan, S. M. Kirtane, and J. K. Sharma, Phys. Rev. B **23**, 2697 (1981).
[26] V. J. Asimov, J. Zaanen, and O. K. Anderson, Phys. Rev. B **44**, 943 (1991).
[27] J. Hugel and M. Kamal, Solid State Commun. **100**, 457 (1996).
[28] I. V. Solovyev and K. Terakura, Phys. Rev. B **58**, 15 496 (1998).
[29] P. Dufek, P. Blaha, V. Sliwko, and K. Schwarz, Phys. Rev. B **49**, 10 170 (1994).
[30] Z. Fang, I. V. Solovyev, H. Sawada, and K. Terakura, Phys. Rev. B **59**, 762 (1999).
[31] W. C. Mackrodt and E. A. Williams, J. Phys.: Condens. Matter **9**, 6591 (1997).
[32] C. Flensburg and D. Madsen, Acta Crystallogr., Sect. A: Found. Crystallogr. **A56**, 24 (2000).
[33] A. Holladay, P. Leung, and P. Coppens, Acta Crystallogr., Sect. A: Cryst. Phys., Diffr., Theor. Gen. Crystallogr. **A38**, 563 (1982).
[34] C. Ballhausen, *Introduction to Ligand Field Theory* (McGraw-Hill, New York, 1962).
[35] P. Coppens, Z. Su, and P. J. Becker, in *International Tables for Crystallography*, 2nd ed., edited by A. J. C. Wilson and E. Prince (Kluwer Academic, Dordrecht, 1999), Vol. C, p. 716.
[36] W. E. Pickett, S. C. Erwin, and E. C. Ethridge, Phys. Rev. B **58**, 1201 (1998).
[37] J. Hubbard and W. Marshall, Proc. Phys. Soc. London **86**, 561 (1965).
[38] F. Keffer and T. Oguchi, Phys. Rev. **115**, 1428 (1959).
[39] P. W. Anderson, *Solid State Physics*, edited by F. Seitz and D. Turnbull (Academic, New York, 1963), Vol. 14, p. 99.
[40] J. C. Slater, *The Self-Consistent Field for Molecules and Solids: Quantum Theory of Molecules and Solids* (McGraw-Hill, New York, 1974), Vol. 4.